



# D-region impact area of energetic particle precipitation during pulsating aurora

Emma Bland<sup>1</sup>, Fasil Tesema<sup>1,2</sup>, and Noora Partamies<sup>1,2</sup>

<sup>1</sup>Department of Arctic Geophysics, University Centre in Svalbard, Longyearbyen, Norway

<sup>2</sup>Birkeland Centre for Space Science, Bergen, Norway

**Correspondence:** Emma Bland (emma.bland@unis.no)

**Abstract.** Ten radars from the Super Dual Auroral Radar Network (SuperDARN) in Antarctica were used to estimate the spatial area over which energetic electron precipitation (EEP) impacts the D-region ionosphere during pulsating aurora (PsA) events. We use an all-sky camera located at Syowa Station to confirm the presence of optical PsA, and then use the SuperDARN radars to detect HF radio attenuation caused by enhanced ionisation in the D-region ionosphere. The HF radio attenuation was identified visually by examining quick-look plots of the background HF radio noise and backscatter power from each radar. The EEP impact area was determined for 74 PsA events. Approximately one third of these events have an EEP impact area that covers at least 12° of magnetic latitude, and three quarters cover at least 4° of magnetic latitude. At the equatorward edge of the auroral oval, 44% of events have a magnetic local time extent of at least 7 hours, but this reduces to 17% at the poleward edge. We use these results to estimate the average size of the EEP impact area during PsA, which could be used as a model input for determining the impact of PsA-related EEP on the atmospheric chemistry.

## 1 Introduction

Pulsating aurorae (PsA) are diffuse auroral emissions which exhibit quasi-periodic brightness fluctuations of about 2–20s (Lessard, 2012; Nishimura et al., 2020). They are commonly observed in the recovery phase of substorms, with greatest occurrence rates in the early morning sector (Jones et al., 2011; Bland et al., 2019; Grono and Donovan, 2020). The energetic electron precipitation (EEP) that produces PsA is thought to arise from chorus wave activity, whereby electrons from the radiation belts are scattered into the atmospheric loss cone (Thorne et al., 2010; Kasahara et al., 2018). The precipitating electrons typically have energies up to the order of 10–100 keV, depositing their energy into the upper mesosphere/lower thermosphere region at approximately 70–120 km altitude (Fang et al., 2008; Turunen et al., 2009; Miyoshi et al., 2010; Tesema et al., 2020b). PsA-related electron density enhancements have been observed at altitudes as low as 68 km, corresponding to electron energies of at least 200 keV (Miyoshi et al., 2015; Turunen et al., 2016; Tesema et al., 2020a).

Due to their high occurrence rates, PsA are thought to be a significant source of ionisation in the upper mesosphere/lower thermosphere region at high latitudes. Impact ionisation by EEP in this region leads to the production of odd-hydrogen ( $\text{HO}_x = \text{OH} + \text{HO}_2$ ) and odd-nitrogen ( $\text{NO}_x = \text{N} + \text{NO} + \text{NO}_2$ ) chemical species, which act as catalysts in ozone depletion reactions. Tesema et al. (2020a) used the one-dimensional Sodankylä Ion-neutral Chemistry model (Verronen et al., 2005; Tu-



25 runen et al., 2009) to show that a typical PsA energy spectrum applied for 120 min causes mesospheric odd-oxygen depletion of 69%. This significant chemical response indicates that PsA-related EEP may also need to be included in atmospheric/climate models such as the Whole Atmosphere Community Climate Model (WACCM) (Marsh et al., 2007) to properly capture the long-term impact of EEP on natural climate variability.

To develop a realistic PsA-related EEP forcing for atmospheric/climate modelling applications, characteristics of PsA such as occurrence rates, durations, energy spectra and spatial coverage need to be determined. PsA occurrence rates and event durations have been determined in several recent studies which used observations from all-sky cameras. The median PsA event duration has been reported to be between 1.4 and 2.25 hours (Jones et al., 2011; Partamies et al., 2017; Bland et al., 2019), and one event lasting for 15 hours was reported by Jones et al. (2013). Jones et al. (2011) and Grono and Donovan (2020) showed that PsA are most common in the morning sector with occurrence rates as high as 86% at around 03:30–06:00 magnetic local time (MLT). Since these occurrence rates were determined using optical data, the authors noted that the results are unreliable after about 06:00 MLT when observation time is restricted by sunlight. Bland et al. (2019) made novel use of the Super Dual Auroral Radar Network (SuperDARN) radar at Syowa Station, Antarctica, to show that D-region ionisation associated with PsA may continue up to about 10:00 MLT, when optical observations are not possible due to daylight.

Our current knowledge of the spatial distribution of PsA comes from a series of studies that used the Time History of Events and Macroscale Interactions during Substorms (THEMIS) all-sky camera network in Canada (Donovan et al., 2006). THEMIS is well-suited to studying the PsA spatial coverage due to its large combined field of view. Grono and Donovan (2019) used three THEMIS cameras and two meridian scanning photometers to determine the upper and lower latitude boundaries of PsA relative to the proton aurora location to identify the source region of the precipitating particle populations. Grono and Donovan (2020) then determined the occurrence probability of PsA as a function of magnetic latitude and MLT. These studies made a distinction between different types of PsA—amorphous PsA (APA), patchy PsA (PPA), and patchy aurora (PA) (see also Grono and Donovan, 2018)—based mainly on the spatial extent and stability of the pulsations, and their motion with the convection. These different PsA types were shown to have different source regions and occurrence distributions. APA was found to have the highest occurrence rate and the widest spatial distribution in both latitude and MLT. APA was the dominant PsA type observed in the pre-midnight sector, whereas all three types were detected in the early morning sector. Yang et al. (2019) reported that APA were associated with stronger cosmic noise absorption enhancements compared to PPA for a fixed auroral brightness. In a larger study using incoherent scatter radar and imaging riometer data, Tesema et al. (2020b) showed that the electron density enhancement below 100 km altitude was greatest for PPA and PA type events, indicating that these precipitating particle populations have higher energies on average compared to APA. Although these conclusions are not consistent, they show that it may be important to distinguish between the different types of PsA when characterizing the middle atmospheric response to EEP.

Grono and Donovan (2019, 2020) have provided new information about the occurrence probability of APA, PPA and PA at different latitudes and MLTs. These results, however, do not provide information about the latitudinal and MLT extent of individual events. This type of spatial coverage information is important for developing a realistic model input. A single PsA event reported by Jones et al. (2013) spanned more than 10 hrs of MLT at its maximum, but this is probably much wider than



60 average. Since optical observations of PsA are possible only during periods of dark, clear skies, it is very difficult to obtain a dataset that is large enough to estimate the statistical spatial coverage of PsA. Furthermore, cameras provide no information about the precipitating particle energy spectrum, or at best they provide very limited information such as the peak emission height (e.g. Partamies et al., 2017). This type of information is important for determining whether an atmospheric chemical response will occur. Tesema et al. (2020a) developed statistical energy spectra for PsA by combining satellite measurements from  
65 253 events, and then used these results to model the atmospheric chemical response to different levels of forcing. They showed that not all PsA have sufficient energy to produce a chemical response. Therefore, PsA occurrence rates and spatial coverage information determined from optical data alone may overestimate the forcing applied to the mesosphere–lower thermosphere region and the resulting chemical response.

The purpose of this study is to estimate the typical area over which PsA-related EEP has sufficient energy to reach mesosphere–  
70 lower thermosphere altitudes ( $\sim 10$ – $200$  keV) and hence produce a chemical response. We shall refer to this area as the *EEP impact area*. To perform this estimate, we use the fact that this higher energy precipitation causes enhanced ionisation in the D-region ionosphere, which in turn attenuates high frequency (HF) radiowaves. This attenuation can be detected using SuperDARN HF radars, as previously shown by Bland et al. (2019). In this study we build upon this work by using ten SuperDARN radars in Antarctica to estimate the EEP impact area for different types of PsA.

## 75 2 Instrumentation

SuperDARN is a global network of 36 HF radars designed primarily for studying high-latitude plasma convection (Greenwald et al., 1995; Chisham et al., 2007; Nishitani et al., 2019). Recently, the radars have also been used to detect HF radio attenuation during shortwave fadeout events (Watanabe and Nishitani, 2013; Berngardt et al., 2018; Chakraborty et al., 2018; Fiori et al., 2018), polar cap absorption events (Bland et al., 2018; Chakraborty et al., 2019), and auroral absorption events including PsA  
80 (Bland et al., 2019). HF radio attenuation events are identified in the SuperDARN radar data as periods of reduced backscatter power combined with a reduction in the background radio noise. The reduced backscatter power is caused by the attenuation of the transmitted radiowaves in the ionosphere, which often reduces the signal strength to below the detection threshold (e.g. Bland et al., 2018). The reduced background noise levels are caused by the attenuation of the background HF radio noise at the radar operating frequency. At the standard SuperDARN operating frequencies of 8–20 MHz, this background radio noise  
85 is produced mainly by lightning activity and propagates around the globe via ionospheric reflections. The noise measurements can be used to estimate the attenuation in decibels relative to a radar-specific quiet day curve using an approach analogous to riometry (Bland et al., 2018; Berngardt, 2020). However, due to the high variability of the noise at the SuperDARN operating frequencies, producing quiet day curves is not straightforward and the methodology is still being developed (Berngardt, 2020). Therefore, in this work we adopt a more qualitative approach based on visual identification of HF attenuation events in quick-  
90 look plots.

In this study we have used ten SuperDARN radars located in Antarctica, and also an all-sky colour digital camera located at Syowa Station. The locations of the radars and the all-sky camera (ASC) are shown in Figure 1. The grey shading and magnetic



local time (MLT) contours in Figure 1 relate to the example event described Section 3. The red circle shows the ASC field of view projected to 100 km height. The radar fields of view are shown in black. For simplicity, we show only the near-range field of view of each radar (180–600 km in range), which is the approximate area where the transmitted radiowaves pass through the D-region ionosphere. Each radar’s total field of view extends to over 3500 km in range, creating significant overlap between the fields of view which is useful for measuring the F region ionospheric convection (e.g. Nishitani et al., 2019, Figure 1b). Each SuperDARN radar consists of a linear array of log-periodic or twin-terminated folded dipole antennas which are phased electronically to produce a beam which can be steered in 16 different azimuthal directions. This beam is narrow in azimuth (3.24°) but has a wide vertical extent (~40°). The 16 beams are scanned sequentially every minute, with a ~3 s integration time for each beam.

SuperDARN radars detect coherent backscatter from electron density structures in the E region and F region ionospheres, and also from the ground following reflection in the ionosphere. The southern hemisphere SuperDARN radars were chosen for this study because they generally detect larger amounts of backscatter on the nightside compared to the northern hemisphere radars. This is probably due to the favorable orientation of the geomagnetic field relative to the radar look directions and geographic latitudes. The near-continuous presence of backscatter on the nightside for most Antarctic radars makes it straightforward to identify periods of reduced backscatter power caused by HF radio attenuation. An example of this procedure is given in Section 3. Note that the three mid-latitude SuperDARN radars located in Australia/New Zealand were not included in this study due to their very large spatial separation from the radars in Antarctica, so they are not shown in Figure 1.

The camera located at Syowa Station is a colour digital camera fitted with a 8mm f/2.8 fisheye lens. The imaging season lasts from April to October, and the camera is programmed to capture images automatically whenever the sun is more than 12° below the horizon. Exposure times are a few seconds, and the image cadence varies from about 6–30s. Daily *keogram* (quick-look) plots are constructed by taking a magnetic north-south slice through the all-sky image and then placing these slices on a time axis. Similarly, an *ewogram* can be constructed using a magnetic east-west slice. PsA can be readily identified in these plots as patchy auroral displays (e.g. Jones et al., 2013; Partamies et al., 2017; Yang et al., 2017), but the original all-sky images are normally required to determine the PsA type (APA, PPA, PA).

### 3 Example event: 14 June 2015

Our method for visually identifying signatures of HF radio attenuation is illustrated using Figure 2. The 12-hour time interval shown commenced at 18:00UT on 13 June 2015. This figure shows the magnetic north-south keogram plot for the all-sky camera at Syowa Station, as well as the background noise and power measurements for each radar with available data. The panels are arranged in order of magnetic latitude, but it should be noted that the radars are located over a wide range of longitudes (see Figure 1). The keograms are identical in both columns. The yellow vertical lines in the keogram plots indicate the onset and end times of a PsA event observed over Syowa Station on 14 June 2015. This is an APA event which occurred in the recovery phase of a substorm. There is a second APA event in this time interval which commences at 04:20UT, but for the purposes of illustrating our event selection we will focus on the first event at 00:40–02:20UT. No data was available from

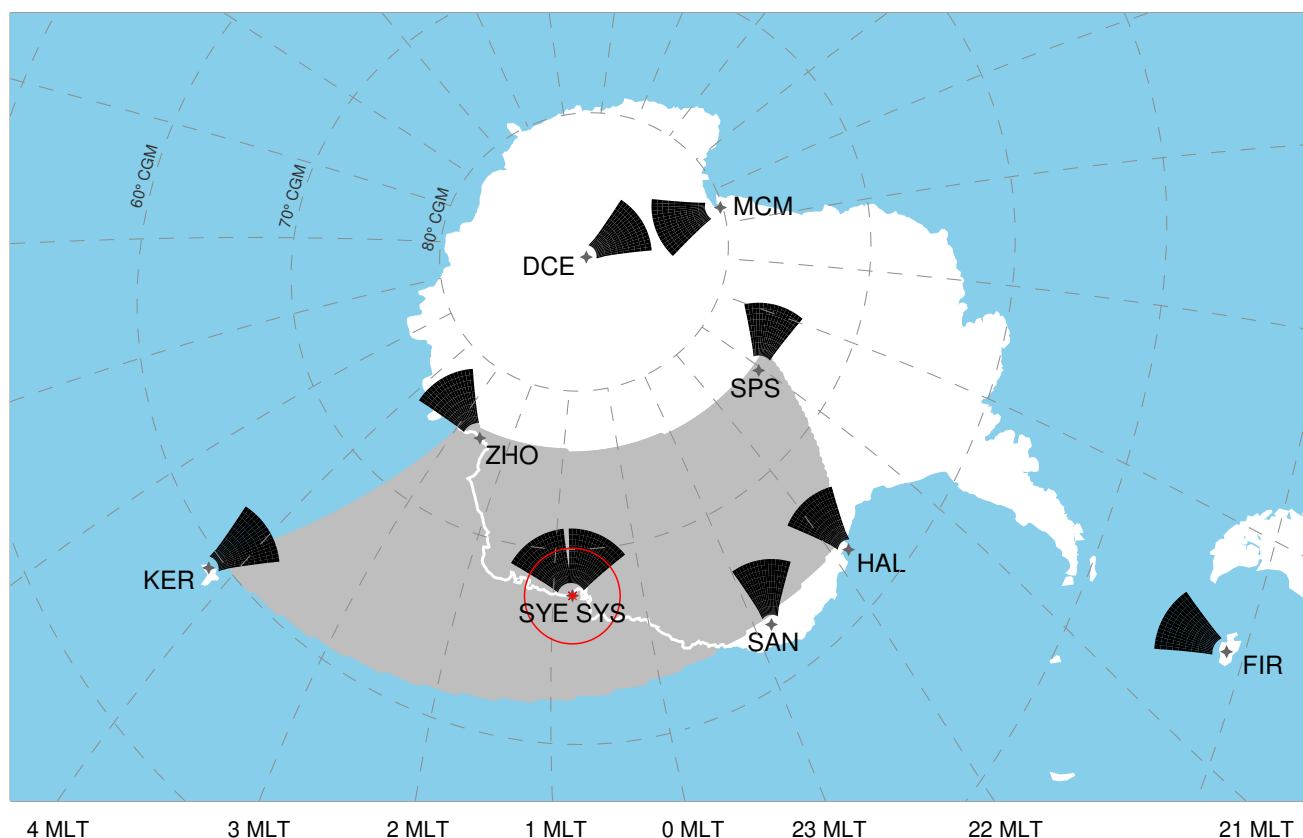


**Figure 1.** Locations and fields of view of the SuperDARN radars and all-sky camera used in this study. Radar fields of view are shown in black, and the camera field of view is shown in red. Only the first 600 km of the radar field of view are shown, as this is the area where the radiowaves are expected to pass through the D-region ionosphere. The grey shading shows the spatial coverage of the energetic electron precipitation impact area for the example pulsating aurora event on 14 June 2015, 00:40–02:20UT. Dashed grey lines indicate corrected geomagnetic (CGM) latitude and magnetic local time (MLT) contours.



either the Falkland Islands (FIR) radar or the SANAE (SAN) radar during this time interval, so they are not included in the figure.

The first column of Figure 2 shows the background noise measurements from each beam of each radar. The noise data have been binned into 10 min intervals and averaged separately in each bin to remove spikes. For most radars there is some variation  
130 in the noise levels between different beams, which may arise from real spatial variations in the atmospheric noise production and ionospheric propagation conditions, or differences in beamforming across the radar field of view. For this work we are not interested in the absolute values of the background noise. Instead we look for sudden changes in the background noise over the entire field of view, which indicate that the HF radio noise has been attenuated in response to enhanced D-region ionisation. For the example event, reduced background noise levels during the PsA event are observed for six out of the eight radars shown,  
135 as indicated by the black vertical lines.

To justify that the reduced background noise measured at the six radar sites was indeed caused by enhanced D-region ionisation, we also study the backscatter power measured by each radar. These measurements are shown in the right column of Figure 2. Each panel shows the raw power levels measured in each 45 km range gate along beam 5. The raw power measurements have arbitrary units and are displayed on a logarithmic scale. High-power values observed across several range gates  
140 simultaneously indicate coherent backscatter returning to the radar from ionospheric electron density irregularities or from the ground. The yellow vertical lines on these plots indicate the time periods for which the background noise was attenuated (determined from the left panel). During these time periods, the backscatter returns from all six radars have reduced power or are completely suppressed. This indicates that the radio waves *transmitted* by the radar have been attenuated. This combination of reduced background noise and reduced backscatter power is strong evidence that the D-region electron density has been  
145 enhanced near the radar site (Bland et al., 2018), and we use these two signatures together in our event selection for this study.

For the example shown in Figure 2, there are two radars that did not detect a clear attenuation signature during the PsA event. These are the McMurdo (MCM) and Dome C East (DCE) radars, located at 80° and 89° corrected geomagnetic (CGM) latitude respectively. For these radars there is neither a clear decrease in the background noise level, nor a reduction in the backscatter power. Note that the background noise at MCM does decrease close to the event onset time. This, however, is accompanied by  
150 an *increase* in the echo power, which indicates that the transmitted radiowaves were not strongly attenuated in the ionosphere. Therefore, the reduced noise at MCM is probably related to the normal diurnal variation in the background noise at the radar site, rather than a response to energetic particle precipitation.

Based on the information in Figure 2, we can now make a rough estimate of the spatial coverage of the EEP impact area for this PsA event. This area is shown by the grey shading in Figure 1, which is the region bounded by the six radars that detected  
155 the event. This area actually represents the minimum EEP impact area for this event. The poleward edge of the EEP impact area extends to at least 75° CGM latitude, where both the South Pole Station (SPS) and Zhongshan (ZHO) radars detected attenuation, but it does not extend as far as the MCM radar at 80° CGM latitude. At the event onset, the SPS and ZHO fields of view were located at 20–21MLT and 03–04MLT respectively, indicating an instantaneous MLT extent of about 7 hr. A similar MLT extent at the equatorward edge of the EEP impact area is inferred from the Halley (HAL) and Kerguelen (KER) radar  
160 pair, extending from ~22–04MLT at the event onset. Since the event was detected at the KER radar site, we can conclude



that the equatorward edge of the EEP impact area extends at least as far as  $60^{\circ}$ CGM latitude in the morning sector. No data were available from the SAN or FIR radars for this event, so we cannot determine whether the EEP impact area extends to the locations of these radars.

It is worth commenting briefly on the nature of background radio noise measurements from SuperDARN radars. The back-  
165 ground noise consists of (1) natural atmospheric radio noise, (2) man-made noise produced by electrical and electronic equip-  
ment near the radar site, and (3) internal noise in the radar receiver system. The short- and long-term variability in the back-  
ground noise depends on the relative contribution of these three sources to the total noise level. EEP-related attenuation signa-  
tures are easiest to identify when the background radio noise exhibits a smooth diurnal variation in the absence of any D-region  
enhancement. In Figure 2, we observe this smooth noise variation in the DCE, MCM, ZHO, SPS and SYE data, and the sudden  
170 reduction in the background noise at the onset of PsA stands out clearly against the slowly-varying background. This diurnal  
variation in the noise is controlled by the global atmospheric noise production and ionospheric propagation conditions. In con-  
trast, the noise measurements from the Halley (HAL) radar are highly variable from one 10 min time bin to the next, and also  
between neighbouring beams, which might arise from either internal receiver noise or man-made noise near the radar site. This  
variability in the noise measurements at Halley makes the visual identification of HF attenuation signatures more difficult. For  
175 this radar, the echo loss from 00:30–02:30 UT is clear (right panel of Figure 2), so we rely more heavily on this parameter to  
determine whether any HF attenuation has occurred. This type of variability in the background noise measurements for some  
radars is a key reason for adopting qualitative event selection criteria in this study, as some judgment regarding the usability of  
the data is required in each case.

#### 4 Event identification for statistical study

180 To select PsA events for our statistical study of the EEP impact area, we began with a list of 102 optical PsA events identified  
visually in keogram plots from the all-sky camera at Syowa Station. This same event list was used by Bland et al. (2019)  
to determine PsA occurrence rates and durations using the SYE SuperDARN radar paired with the all-sky camera data. The  
optical PsA events were classified as APA, PPA or PA by visually studying the keogram and ewogram plots, and also the 10 s-  
cadence all-sky images for each event. The pulsating auroral structures that we used to distinguish between the different types  
185 are described in detail by Grono and Donovan (2018) and Yang et al. (2019). APA are identified as transient pulsating emissions  
with no persistent structure or sense of average motion. In contrast, PPA and PA consist of quasi-stable auroral patches that  
last for tens of minutes and can be tracked across the camera field of view. For PA, pulsations are observed only within a small  
portion of the emission, such as near the edges, whereas for PPA the pulsations are observed over a much larger area. For  
56 events in our list, one dominant type of PsA was observed throughout the whole event. For the remaining 18 events, the  
190 dominant type of PsA changed part-way through the event. For these events, we classified them based on the first type of PsA  
that was observed. There were only three events during which PA were observed, and in all cases the PA were preceded by  
APA so they were classified as APA. Note that our PsA classifications apply only to Syowa Station, as we cannot determine the

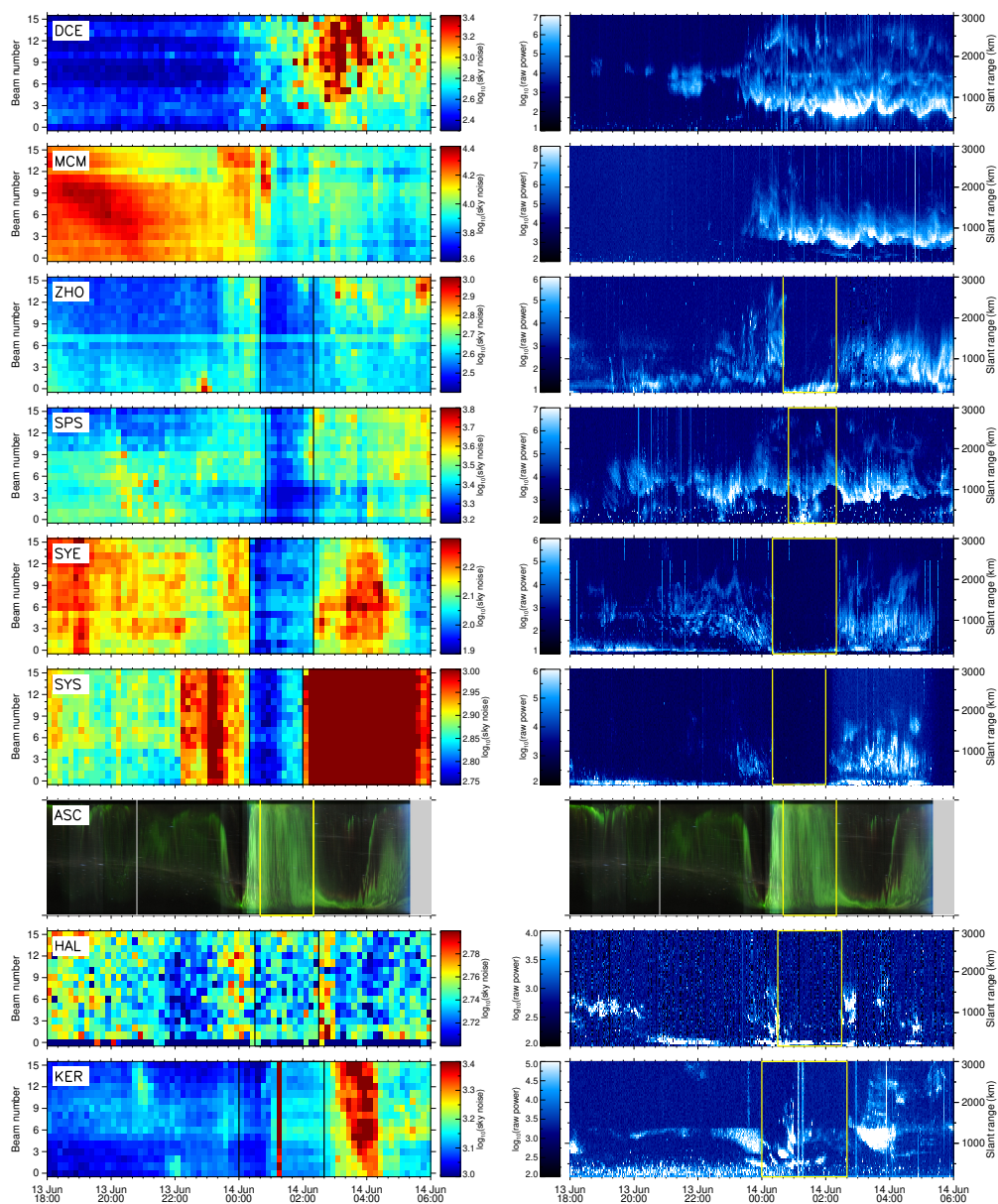


**Figure 2.** Quick-look plots showing the background ‘sky’ noise (left) and raw echo power (right) parameters for eight SuperDARN radars from 13–14 June 2015. The magnetic north-south keogram from the all-sky camera (ASC) at Syowa Station is also shown in both columns. The event start and end times are marked using black/yellow vertical lines.



PsA type from the radar data. Due to this limitation, this study is designed to detect periods of enhanced D-region ionisation that occur simultaneously with different types of optical PsA observed at Syowa Station.

195 Quick-look plots similar to Figure 2 were produced for each PsA event in the list. For each radar we determined whether the background noise measurements and the echo power had been attenuated based on a visual inspection of the data. Often there was some uncertainty about whether a given radar had (or had not) detected an EEP signature. To capture this uncertainty, the attenuation for each radar was classified as *clearly observed/not observed* or *probably observed/not observed*. If we could not determine the presence or absence of an attenuation signature either way for a given event, that radar was excluded from  
200 the analysis. For an event to be included in this study, we required that at least one radar in addition to the Syowa Station instrumentation had data available with sufficient quality to determine whether an attenuation signature was present. The final event list contained 74 events detected during the 2011, 2013 and 2015 Antarctic winter seasons. For each event we recorded the following information:

- The availability of data from each radar;
- 205 – The start time and end time of the attenuation at each radar site (if observed);
- A classification of our uncertainty in whether or not any HF attenuation had occurred at each radar site.

In most cases, the onset times for each radar that detected the event are within 30 minutes of the onset times recorded for the SYE radar. For a few events, the onset times at ZHO, KER or SPS are delayed 1–3 hours after the onset at SYE, but there is still considerable temporal overlap between the two sites. This might indicate a latitudinal expansion of the EEP impact area  
210 as the event evolves. Similarly, there are three events where the HAL or KER radars detected attenuation more than one hour before the onset at SYE, which might indicate that the particle precipitation began at lower latitudes and later expanded over Syowa Station.

In this study we have used the all-sky camera at Syowa Station to determine the presence of optical PsA. Since HF attenuation will occur in response to any process that enhances the D-region ionisation, we cannot confirm that the attenuation signatures  
215 observed by the radars were caused by PsA specifically. For example, the attenuation observed by the SYE and SYS radars in Figure 2 commences at substorm onset at 00:20 UT, about 20 min before optical PsA are visible in the keogram. This is very typical since PsA are frequently observed in the substorm recovery phase, so the onset times determined from the radar data will often be 10–30 minutes earlier than the onset of optical PsA (Bland et al., 2019). To increase the chances that the attenuation signatures at all radar sites are due to PsA-related EEP, we require that the attenuation observed by any individual radar lasts  
220 for at least 1 hr to qualify as a positive event identification at that site. Since substorm expansion phases are relatively short (Juusola et al., 2011; Partamies et al., 2013), this criterion should eliminate brief attenuation enhancements during substorm expansion phases that are not accompanied by PsA in the recovery phase.

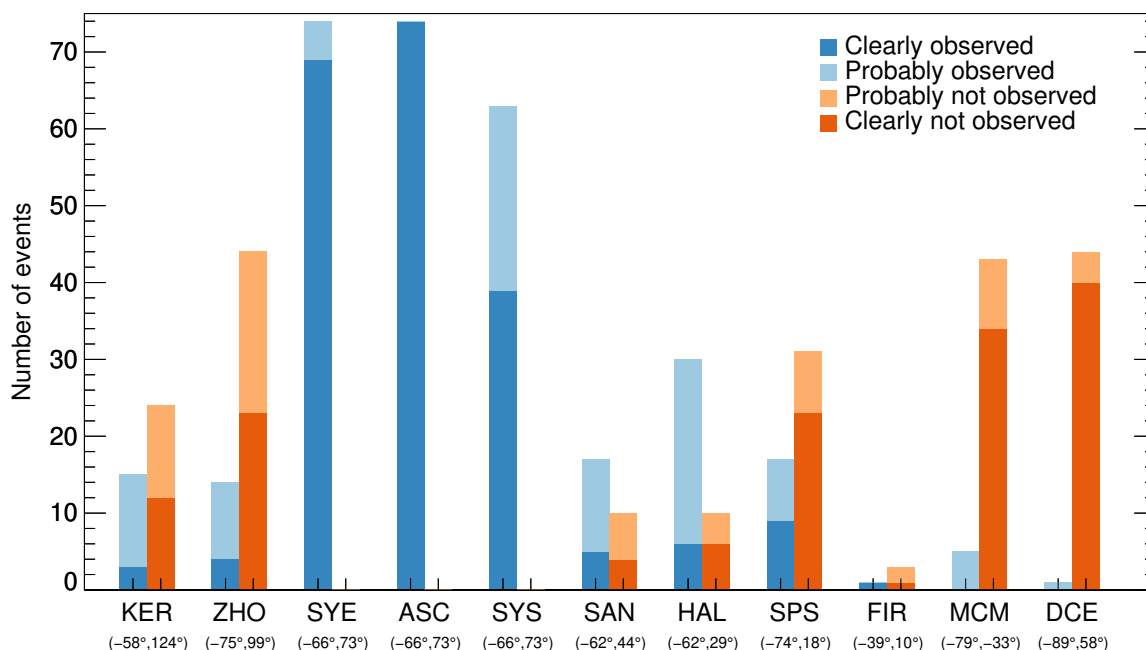


**Figure 3.** Number of events observed and not observed by each radar and the all-sky camera (ASC). Corrected geomagnetic coordinates are given in brackets.

## 5 Results

Figure 3 is a bar graph showing the number of events detected and not detected by each radar. Colour coding is used to represent our uncertainty in determining whether any HF attenuation had occurred. The all-sky camera (ASC) is also included in this plot, with all 74 events clearly present. The SYE and SYS radars detected attenuation during all events for which data were available (74 and 63 events respectively). For the SYE radar, 5 of these events had some evidence of HF attenuation but this signature was less clear compared to the other events. For the KER and HAL radars, most of the positive and negative identifications of HF attenuation were uncertain due to the variability of the background noise and lower backscatter occurrence for these radars, similar to Figure 2. The MCM and DCE radars rarely detect any attenuation during the PsA events. These two radars had good data availability, high echo occurrence, and the background noise exhibits smooth diurnal variations, so we conclude that the EEP impact area rarely extends to these latitudes. The lowest latitude radar, FIR, had very limited data availability, so it is not possible to draw conclusions about the EEP response at that location.

To get a general overview of the spatial coverage of the PsA events, it is helpful to first consider only those events that had data available from most of the radars. Therefore, we now take the subset of events with data available from at least five of the following six radars: [HAL, KER, SAN, SPS, SYE, ZHO]. These radars cover the spatial region extending from 58°

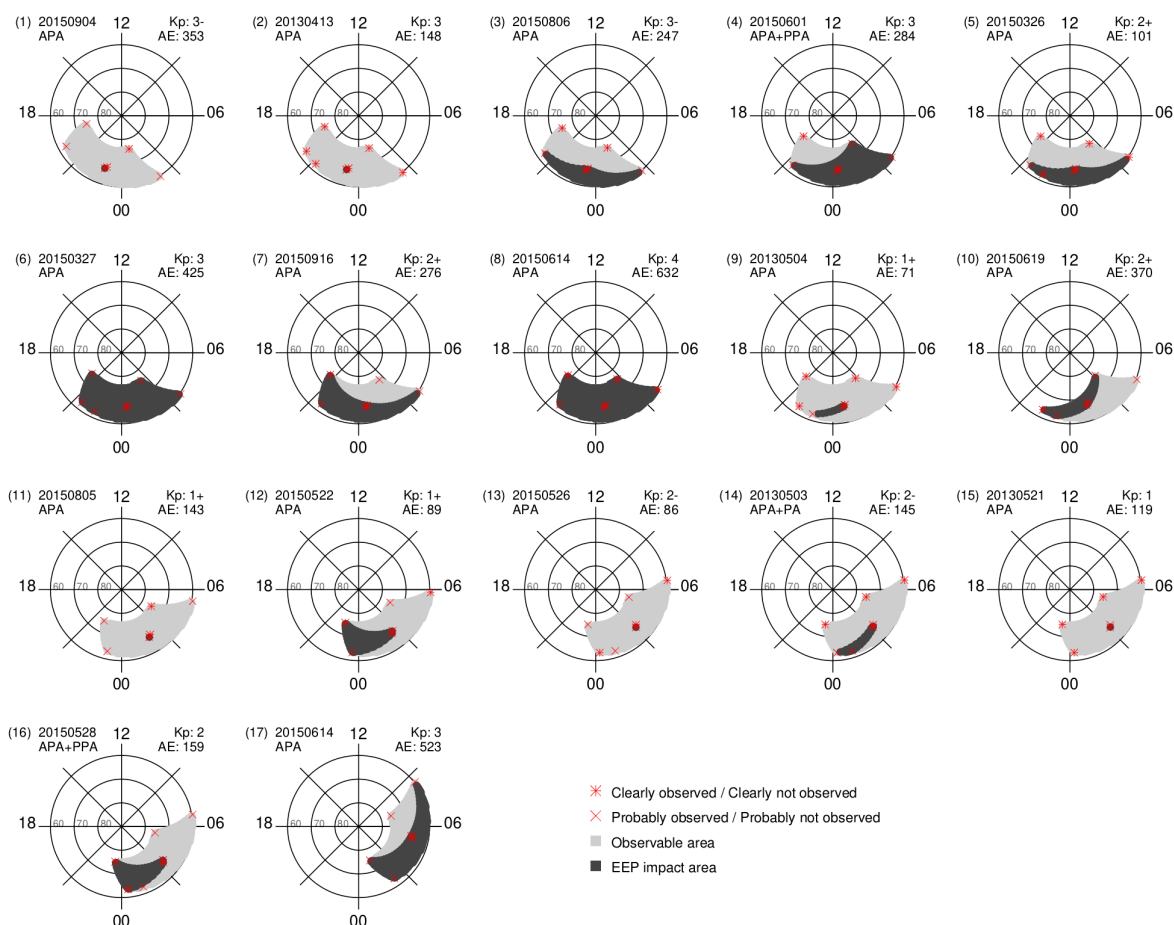


**Figure 4.** EEP impact area for amorphous pulsating aurora (APA) events with data available from at least five radars. The dark grey shading shows the EEP impact area, and the light grey shading shows the region bounded by the radars that did not detect any attenuation. Red symbols are used to indicate our uncertainty in determining whether any attenuation had occurred.

to  $74^\circ$  magnetic latitude over a  $106^\circ$ -wide magnetic longitudinal sector. The DCE and MCM radars are not included in this list because the event detection rate at these sites was close to zero. The FIR radar was also excluded due to the low data availability.

240 In total, there were 17 APA and 10 PPA events with data available from at least five of the six radars listed above, and the EEP impact area for these events is shown in Figures 4 and 5 respectively. For events where the PsA type changed during the event, we grouped the events according to the PsA type observed at the event onset. The events have been sorted and numbered according to the magnetic local time of the event onset at SYE. The light grey shading shows the region bounded by all radars with available data, and then a portion of this area is shaded dark grey to show the region in which attenuation was detected.

245 The red symbols are used to indicate our uncertainty in whether attenuation occurred or did not occur at each radar site. Since

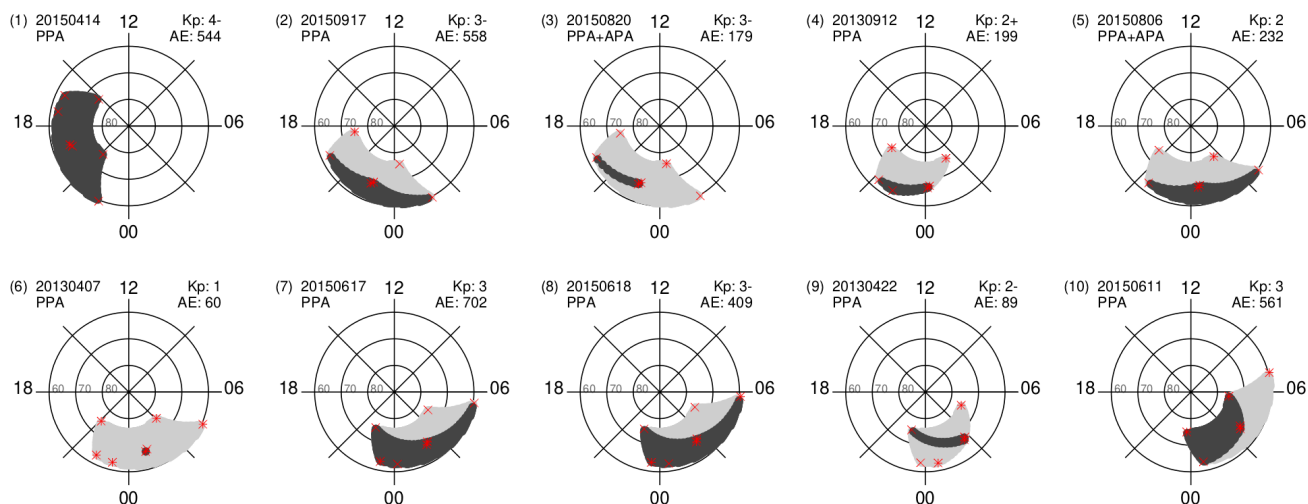


**Figure 5.** Same as Figure 4, but for patchy pulsating aurora (PPA).

the event onset times are slightly different for each radar, we use the dark grey shading to represent the total area over which attenuation was observed during the event. The auroral electrojet (AE) index and the planetary K-index (Kp) values at the event onset time are also shown, and we note that there is no obvious correlation between geomagnetic activity and the size of the EEP impact area.

250 Two APA events and one PPA event were detected by all radars simultaneously (dark grey shading only). For these events, the EEP impact area extended over a minimum of 7 hr of MLT and  $16^\circ$  of magnetic latitude. For the remaining events, the latitude or MLT boundary of the EEP impact area can be identified. For example, APA events #3 and #5 are confined to the  $\sim 60\text{--}70^\circ$  CGM latitude range. There are also many events that do not extend over the entire observable MLT range, such as APA event #9 and PPA event #3. Five APA events and one PPA event were observed only at Syowa Station. For these events,  
255 we conclude that the EEP impact area is narrow in both latitudinal and longitudinal extent. Since the radar coverage is very sparse, we checked all-sky camera data from Syowa Station to determine the spatial coverage of the optical PsA for these events. For all events detected only by the Syowa Station radars, the latitudinal extent of the optical PsA was narrower than the camera field of view. We show an example of this in Figure 6 for APA event #2, where the optical PsA covers about half of the north-south field of view. We found no examples where the east-west extent of the optical PsA was smaller than the camera  
260 field of view.

The results presented in Figures 4 and 5 show that the EEP impact area associated with PsA events can vary significantly. However, due to the limited number of events that met our data availability criteria, it is difficult to draw conclusions about the average EEP impact area based on these results. Therefore, we now use the observations from all 74 events to build a statistical description of the EEP impact area. These results are presented in Figure 7 using a format similar to a correlation

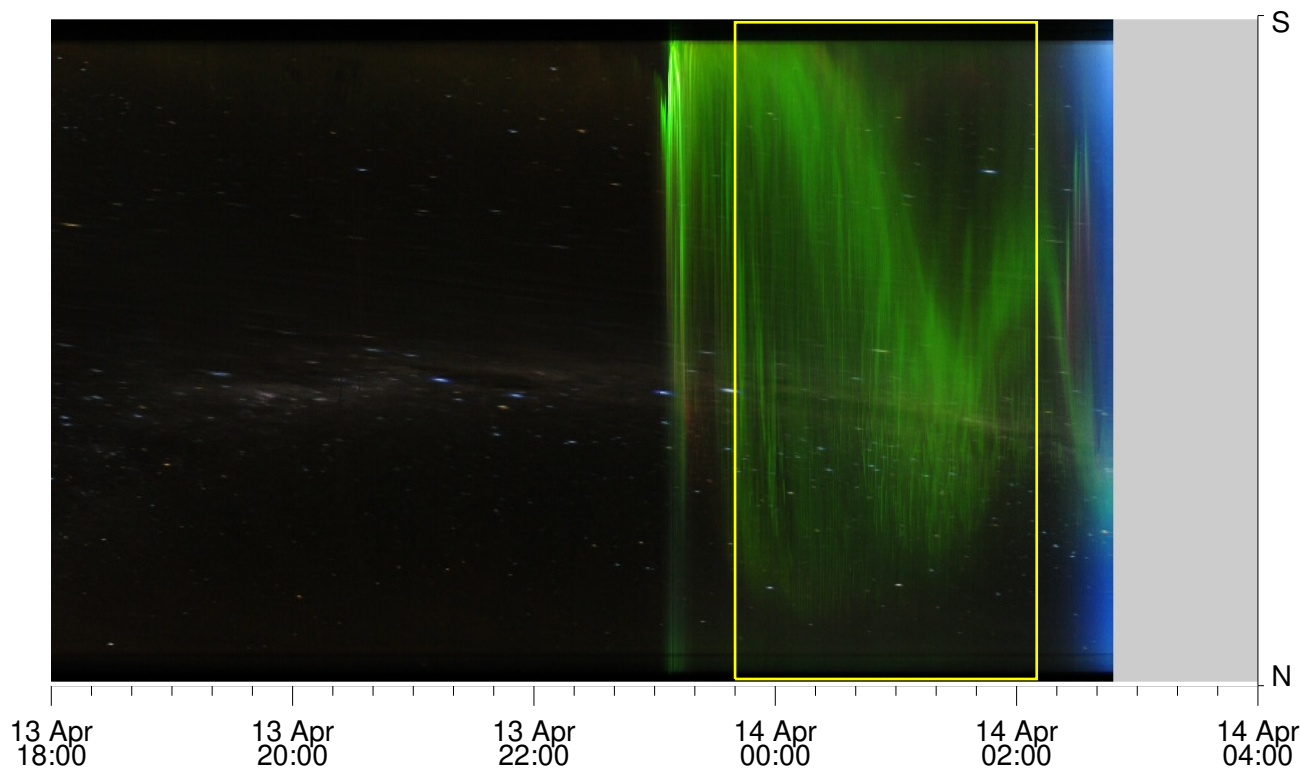


**Figure 6.** Magnetic north-south (N-S) keogram from the all-sky camera at Syowa Station for the period 13–14 April 2013. The yellow box indicates the time period when pulsating aurora was observed.

265 matrix. Each cell shows the percentage of optical PsA events that were accompanied by an attenuation signature from both  
 radars corresponding to that cell. For example, 36% of the optical PsA events were accompanied by an attenuation signature  
 from both the HAL and SPS radars simultaneously. The percentage occurrence for the all-sky camera (ASC) paired with each  
 individual radar is also included in the figure. The cells are colour-coded according to these percentages, and the numerical  
 value is provided in each cell. The total number of events used to calculate the percentage is given in parentheses. The total  
 270 number of events varies widely between radar pairs because there were many events for which data were not available from  
 both radars simultaneously. The radars/ASC are sorted according to magnetic longitude, except for DCE which is placed to the  
 far right/top of the plot. The geomagnetic coordinates for each instrument are shown below each 3-letter radar/camera code.  
 Cells with a dark blue outline identify instrument pairs that are separated by less than  $5^\circ$  of magnetic latitude, which are useful  
 for estimating the longitudinal extent of the EEP impact area at a particular latitude. Similarly, cells with a light blue outline  
 275 identify radar pairs that are separated by less than  $15^\circ$  of magnetic longitude and can be used to estimate the latitudinal extent  
 of the EEP impact area.

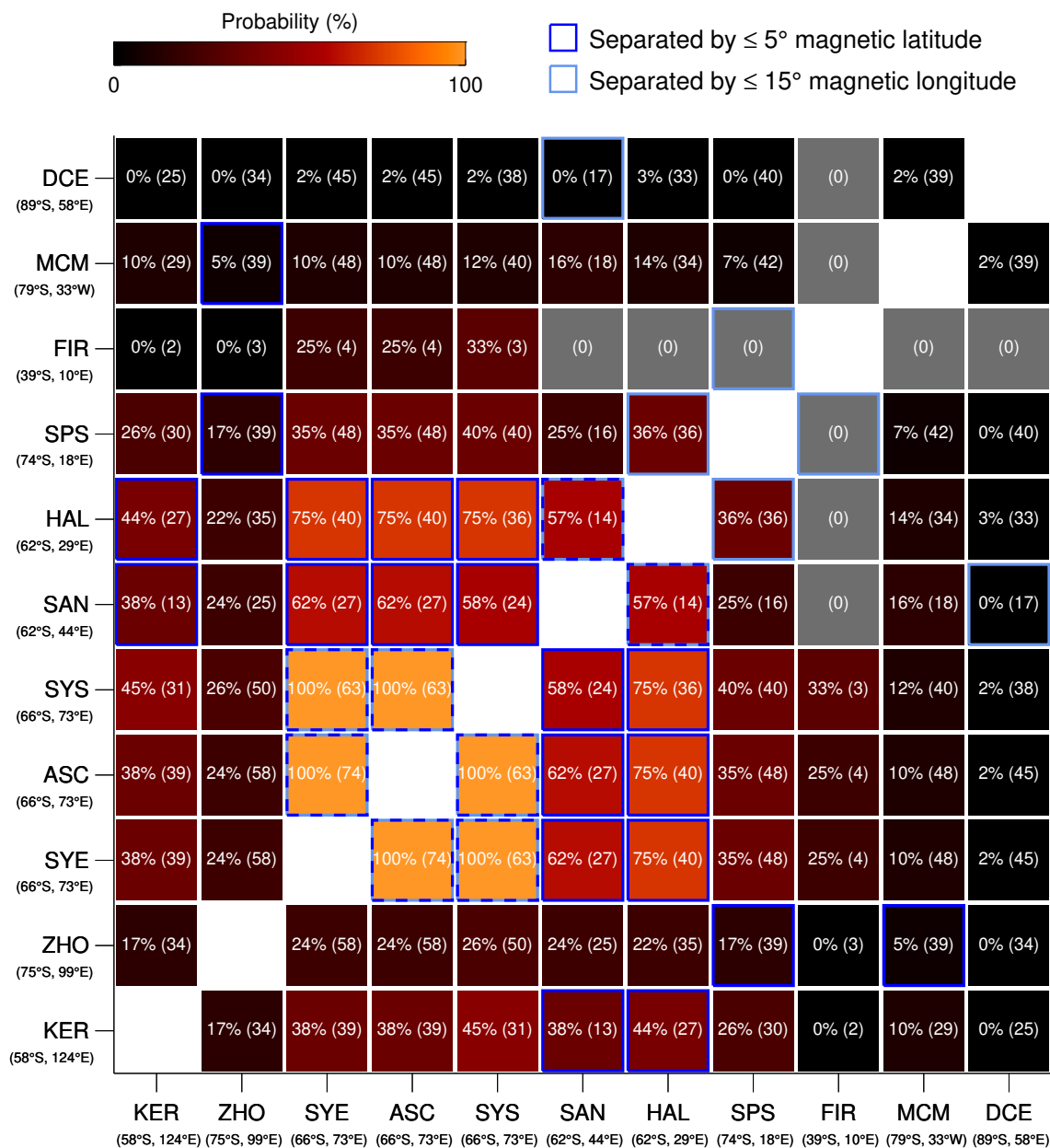


**Figure 7.** Probability of detecting HF radio attenuation for each pair of SuperDARN radars. In all cases, optical PsA were also detected simultaneously at Syowa Station. The white text shows the probabilities for each radar pair, and the number of events used to calculate this probability is given in brackets. The box shading is used to represent these probabilities visually. Boxes with a light blue outline indicate radar pairs which have a similar magnetic latitude, and the darker blue outline indicates the co-located instruments at Syowa Station. The corrected geomagnetic coordinates for each radar are given in brackets below each 3-letter station ID. The probabilities for the all-sky camera (ASC) paired with each radar are also shown.



We will first discuss the probability that each radar detects HF attenuation simultaneously with optical PsA at Syowa Station. 100% of the optical PsA events at Syowa Station were accompanied by HF attenuation at SYE and SYS. This is expected because these instruments have similar fields of view. The HAL radar, which is located at a similar magnetic latitude to Syowa  
280 Station but  $44^\circ$  to the west, detected HF attenuation with 75% probability. For radars near the poleward edge of the auroral oval, we see that 24% of the optical PsA events were accompanied by attenuation at ZHO ( $75^\circ$  latitude), and this drops to just 10% at  $80^\circ$  latitude (MCM radar). For the lowest magnetic latitude station, FIR, data were available for just four events, and the radar detected attenuation for only one of these events, so the 25% occurrence rate for this radar is unreliable.

The KER–HAL and SPS–ZHO radar pairs provide information about the MLT extent of the EEP impact area near the  
285 equatorward and poleward edges of the auroral oval respectively. The KER and HAL radars, located at  $58\text{--}62^\circ$  latitude, both detected attenuation for 44% of the PsA events. This radar pair is separated by  $\sim 6$  hr of MLT. At the poleward edge of the auroral oval ( $\sim 75^\circ$ ), 17% of events were detected by both the SPS and ZHO radars, which have a 7 hr MLT separation. We conclude from these results that the MLT extent of the EEP impact area is, on average, larger at the equatorward edge of the auroral oval.

290 The HAL–SPS radar pair provides information about the latitudinal extent of the EEP impact area to the west of our reference location at Syowa Station. This pair detected HF attenuation simultaneously with probability 36%. East of the reference location, the ZHO–KER radar pair detected HF attenuation simultaneously with probability 17%. The SPS–HAL and ZHO–KER pairs do not have the same latitudinal spacing, so it is not appropriate to compare the probabilities between these pairs. However, both results indicate that the latitudinal extent of the EEP impact area is less than  $12^\circ$  for the majority of events.

## 295 6 Discussion

The results presented in this study provide some basic estimates of the EEP impact area during pulsating aurora events. This type of information is necessary for developing realistic inputs to atmospheric models that are used to study the impact of EEP on the middle atmospheric chemistry and the contribution of EEP forcing to natural climate variability. Our results show that 36% of PsA events extend over at least  $12^\circ$  of magnetic latitude (SPS–HAL pair), and  $\sim 60\text{--}75\%$  extend over at least  $4^\circ$   
300 of magnetic latitude (SYE–SAN and SYE–HAL pairs). At the equatorward edge of the auroral oval, 44% of events have a magnetic local time extent greater than 7 hours (KER–HAL pair). At the poleward edge, 17% of events cover this MLT range (ZHO–SPS pair).

The number of events used to calculate the above probabilities is relatively low, ranging from 27 to 39, and it is even lower for some other radar pairs shown in Figure 7. In addition, this study only includes PsA events that were detected at Syowa Station,  
305 which may contribute to the different MLT extent results observed at different latitudes. To determine whether our results are realistic, we can make some simple comparisons with earlier work. In particular, Grono and Donovan (2020) showed that optical APA occur over a wider MLT range at  $\sim 65^\circ$  latitude compared to  $\sim 75^\circ$  latitude. Although their study did not provide information about the instantaneous spatial coverage of optical PsA, it is consistent with our finding that the MLT extent of the EEP impact area is larger on average at  $65^\circ$  latitude, where 44% of events covered at least 7 hours MLT (KER–HAL pair)



310 compared to 17% at 75° latitude (SPS–ZHO pair). We also conclude that the optical PsA event reported by Jones et al. (2013) is probably quite rare. For that event, optical PsA were observed over 10 hours of MLT, but our results indicate that a large majority of PsA events have an impact area covering less than 7 hours of MLT. It is possible, however, that the EEP impact area is smaller than the spatial area over which optical PsA are observed. This could be investigated further using the SuperDARN radars and riometers in North America combined with simultaneous observations from the THEMIS all sky cameras.

315 In terms of magnetic latitude coverage, Grono and Donovan (2020) report that APA occur in the magnetic latitude range 56–75°, whereas PPA and PA occur over slightly narrower ranges of 57–73° and 59–74° respectively. They reported that the APA occurrence probability above about 74° was  $\lesssim 15\%$ , and zero for PPA and PA. For our study, observations from the SPS–SYE and ZHO–SYE radar pairs indicate that the EEP impact area regularly extends as far as  $\sim 75\text{--}77^\circ$  latitude (35% and 24% respectively). Although Grono and Donovan (2020) reported zero occurrence of optical PPA and PA at these latitudes, there  
320 are several PPA events in our dataset for which HF attenuation was detected by the ZHO or SPS radars. In particular, events #1, #7 #8, #9 and #10 in Figure 5, which is half of the events shown in that figure. Kp and AE indices for these PPA events are higher than for the other PPA events, which would play a role in determining the size and location of the EEP impact area. Differences in the auroral oval location between the northern and southern hemispheres may also contribute to the different latitudinal coverage results in this study compared to Grono and Donovan (2020). We also note that the PsA type classification  
325 was determined only at Syowa Station, and it is likely that other PsA types were present elsewhere for many events.

Based on the results described above, we can make a rough estimate of the average EEP impact area that could be used as input to an atmospheric model such as WACCM (Marsh et al., 2007; Verronen et al., 2016). As described above, the majority of events cover less than 7 hours of MLT. From the SYE, SYS, KER, SAN and HAL pair combinations shown in Figure 7, we determine that roughly half of the PsA events have an instantaneous MLT coverage of at least 2–3 hours at  $\sim 65^\circ$  magnetic  
330 latitude. Therefore, the average MLT extent at this latitude is probably around 4–5 hours. The average MLT extent is much narrower at  $\sim 75^\circ$  magnetic latitude, with the large majority (65–76%) of events covering less than 2–4 hours simultaneously (SYE–SPS and SYE–ZHO pairs). PsA occurrence rates reach a maximum in the early morning sector, at about 04:00MLT (Jones et al., 2011; Bland et al., 2019; Grono and Donovan, 2020), and this result could be used to centre the EEP impact area in a model PsA forcing. The average latitudinal extent of the EEP impact area is difficult to estimate due to the very  
335 sparse latitudinal coverage of the SuperDARN radars, and the latitude dependence of PsA occurrence. We have determined that approximately one third of the events cover 12° of latitude to the west of Syowa Station (SPS–HAL pair), so the median latitudinal extent would be a few degrees narrower. By combining this result with the latitude-dependent optical PsA occurrence rates (Grono and Donovan, 2020, Fig. 5), one could reasonably assume that the average EEP impact area covers the magnetic latitude range of about 62–70°.

340 The four most important radars for estimating the EEP impact area in our study are KER, ZHO, SPS and HAL. These radars provide observations from the equatorward and poleward edges of the auroral oval over a wide longitudinal area. Unfortunately, the HAL radar ceased operations in 2015, so it was not possible to extend the dataset to include more recent events from that location. Although the dataset from the other radars could potentially be expanded to include more events, it may be more fruitful to repeat this analysis using the North American SuperDARN radars, which provide additional coverage from a larger



345 number of radars and can potentially be compared with optical PsA observations from the THEMIS all-sky cameras. The southern hemisphere data were used in this study because they generally detect large amounts of backscatter on the nightside, which makes it straightforward to identify periods of reduced backscatter power. We speculate that the high echo occurrence for the southern hemisphere radars is due to the low operating frequencies used and more favourable geometry with the magnetic field for satisfying the aspect-angle condition for ionospheric scatter detection. Also, the southern hemisphere radars generally  
350 operate at just one or two frequencies, which makes it easier to identify attenuation signatures in the background radio noise, which is frequency-dependent. With an improved understanding of the background radio noise measured by SuperDARN radars, it may be possible to reliably identify HF attenuation events using only the background noise parameter. This would improve the suitability of the North American SuperDARN radars to estimating the EEP impact area.

Since our event detection procedure is qualitative, we cannot draw conclusions about the magnitude of the D-region electron  
355 density enhancements. This may be possible in the future with improved baselining of the background noise parameter (e.g. Bergardt, 2020), and a better understanding of the sensitivity of SuperDARN radars to PsA-related EEP. For the purposes of atmospheric modelling, however, statistical EEP energy spectra from satellite observations (e.g. Tesema et al., 2020b) would probably provide a more accurate estimate the relative impact of different types of PsA than what is possible with the SuperDARN radars.

## 360 7 Conclusions

The spatial extent of the EEP impact area during 74 pulsating aurora events has been estimated using observations of HF radio attenuation from ten SuperDARN radars in Antarctica. We defined the EEP impact area as the horizontal region over which PsA-related EEP has sufficient energy to cause a detectable amount of HF attenuation in the D-region ionosphere. This represents the area over which PsA-related EEP may cause an atmospheric chemical response. For 75% of the events studied,  
365 the EEP impact area extended over at least 4° of magnetic latitude, and 36% of events extended over at least 12° of magnetic latitude. The MLT extent was found to be larger on average at lower latitudes compared to higher latitudes. Based on our results, and earlier work using optical data, we estimated the average EEP impact area for PsA that could be used as input to an atmospheric model such as WACCM. This average EEP impact area extends from about 62–70° magnetic latitude and covers about 4–5 hours of MLT. We emphasise that the SuperDARN radars have sparse spatial coverage, so these results provide only  
370 a rough estimate of the average EEP impact area.

*Data availability.* The SuperDARN data were obtained from the British Antarctic Survey data mirror (<https://www.bas.ac.uk/project/superdarn>). The all sky camera data are available at [http://polaris.nipr.ac.jp/~acaaurora/syowa\\_CDC\\_QL/](http://polaris.nipr.ac.jp/~acaaurora/syowa_CDC_QL/). Geomagnetic activity indices were obtained from the GSFC/SPDF OMNIWeb interface at <https://omniweb.gsfc.nasa.gov>.



*Author contributions.* The SuperDARN data analysis was done by EB. NP provided the original PsA event list from Syowa Station and FT  
375 performed the classification. All authors have contributed to the discussion of the results and the writing of the paper.

*Competing interests.* The authors declare no competing interests

*Acknowledgements.* EB is supported by the Research Council of Norway (NRC) under contract 287427. NP and FT are supported by the  
NRC under CoE contract 223252. The authors acknowledge the use of SuperDARN data. SuperDARN is a collection of radars funded by the  
national scientific funding agencies of Australia, Canada, China, France, Italy, Japan, Norway, South Africa, United Kingdom and United  
380 States of America. We thank H. Miyaoka, National Institute of Polar Research (NIPR), Japan, for providing the data from the all sky colour  
digital camera at Syowa Station. This camera is part of the Science Program of the Japanese Antarctic Research Expedition and NIPR.



## References

- Berngardt, O. I.: Noise level forecasts at 8–20MHz and their use for morphological studies of ionospheric absorption variations at EKB ISTP SB RAS radar, *Advances in Space Research*, <https://doi.org/10.1016/j.asr.2020.04.005>, 2020.
- 385 Berngardt, O. I., Ruohoniemi, J. M., Nishitani, N., Shepherd, S. G., Bristow, W. A., and Miller, E. S.: Attenuation of decameter wavelength sky noise during x-ray solar flares in 2013–2017 based on the observations of midlatitude HF radars, *Journal of Atmospheric and Solar-Terrestrial Physics*, <https://doi.org/10.1016/j.jastp.2018.03.022>, 2018.
- Bland, E. C., Heino, E., Kosch, M. J., and Partamies, N.: SuperDARN Radar-Derived HF Radio Attenuation During the September 2017 Solar Proton Events, *Space Weather*, 16, <https://doi.org/10.1029/2018SW001916>, 2018.
- 390 Bland, E. C., Partamies, N., Heino, E., Yukimatu, A. S., and Miyaoka, H.: Energetic Electron Precipitation Occurrence Rates Determined Using the Syowa East SuperDARN Radar, *Journal of Geophysical Research: Space Physics*, 124, 6253–6265, <https://doi.org/10.1029/2018JA026437>, 2019.
- Chakraborty, S., Ruohoniemi, J. M., Baker, J. B. H., and Nishitani, N.: Characterization of Short-Wave Fadeout seen in Daytime SuperDARN Ground Scatter Observations, *Radio Science*, 53, <https://doi.org/10.1002/2017RS006488>, 2018.
- 395 Chakraborty, S., Baker, J. B. H., Ruohoniemi, J. M., Kunduri, B., Nishitani, N., and Shepherd, S. G.: A Study of SuperDARN Response to Co-occurring Space Weather Phenomena, *Space Weather*, 17, 1351–1363, <https://doi.org/10.1029/2019SW002179>, 2019.
- Chisham, G., Lester, M., Milan, S. E., Freeman, M. P., Bristow, W. A., Grocott, A., McWilliams, K. A., Ruohoniemi, J. M., Yeoman, T. K., Dyson, P. L., Greenwald, R. A., Kikuchi, T., Pinnock, M., Rash, J. P. S., Sato, N., Sofko, G. J., Villain, J. P., and Walker, A. D. M.: A decade of the Super Dual Auroral Radar Network (SuperDARN): Scientific achievements, new techniques and future directions, *Surveys in Geophysics*, 28, 33–109, <https://doi.org/10.1007/s10712-007-9017-8>, 2007.
- 400 Donovan, E., Mende, S., Jackel, B., Frey, H., Syrjäsoo, M., Voronkov, I., Trondsen, T., Peticolas, L., Angelopoulos, V., Harris, S., et al.: The THEMIS all-sky imaging array—System design and initial results from the prototype imager, *Journal of Atmospheric and Solar-Terrestrial Physics*, 68, 1472–1487, 2006.
- Fang, X., Randall, C. E., Lummerzheim, D., Solomon, S. C., Mills, M. J., Marsh, D. R., Jackman, C. H., Wang, W., and Lu, G.: Electron impact ionization: A new parameterization for 100 eV to 1 MeV electrons, *Journal of Geophysical Research: Space Physics*, 113, <https://doi.org/10.1029/2008JA013384>, 2008.
- 405 Fiori, R. A. D., Koustov, A. V., Chakraborty, S., Ruohoniemi, J. M., Danskin, D. W., Boteler, D. H., and Shepherd, S. G.: Examining the potential of the Super Dual Auroral Radar Network for monitoring the space weather impact of solar X-ray flares, *Space Weather*, 16, 1348–1362, 2018.
- 410 Greenwald, R. A., Baker, K. B., Dudeney, J. R., Pinnock, M., Jones, T. B., Thomas, E. C., Villain, J. P., Cerisier, J. C., Senior, C., Hanuise, C., Hunsucker, R. D., Sofko, G. J., Koehler, J., Nielsen, E., Pellinen, R., Walker, A. D. M., Sato, N., and Yamagishi, H.: DARN/SuperDARN: A Global View of the Dynamics of High-Latitude Convection, *Space Science Reviews*, 71, 761–796, <https://doi.org/10.1007/BF00751350>, 1995.
- Grono, E. and Donovan, E.: Differentiating diffuse auroras based on phenomenology, *Annales Geophysicae*, 36, 891–898, 2018.
- 415 Grono, E. and Donovan, E.: Constraining the Source Regions of Pulsating Auroras, *Geophysical Research Letters*, 46, 10 267–10 273, 2019.
- Grono, E. and Donovan, E.: Surveying pulsating auroras, *Annales Geophysicae*, 38, 1–8, 2020.
- Jones, S. L., Lessard, M. R., Rychert, K., Spanswick, E., and Donovan, E.: Large-scale aspects and temporal evolution of pulsating aurora, *Journal of Geophysical Research: Space Physics*, 116, <https://doi.org/10.1029/2010JA015840>, 2011.



- Jones, S. L., Lessard, M. R., Rychert, K., Spanswick, E., Donovan, E., and Jaynes, A. N.: Persistent, widespread pulsating aurora: A case  
420 study, *Journal of Geophysical Research: Space Physics*, 118, 2998–3006, <https://doi.org/10.1002/jgra.50301>, 2013.
- Juusola, L., Østgaard, N., Tanskanen, E., Partamies, N., and Snekvik, K.: Earthward plasma sheet flows during substorm phases, *Journal of  
Geophysical Research: Space Physics*, 116, <https://doi.org/10.1029/2011JA016852>, 2011.
- Kasahara, S., Miyoshi, Y., Yokota, S., Mitani, T., Kasahara, Y., Matsuda, S., Kumamoto, A., Matsuoka, A., Kazama, Y., Frey, H., et al.:  
Pulsating aurora from electron scattering by chorus waves, *Nature*, 554, 337, 2018.
- 425 Lessard, M. R.: A review of pulsating aurora, *Auroral phenomenology and magnetospheric processes: Earth and other planets*, pp. 55–68,  
2012.
- Marsh, D., Garcia, R., Kinnison, D., Boville, B., Sassi, F., Solomon, S., and Matthes, K.: Modeling the whole atmosphere re-  
sponse to solar cycle changes in radiative and geomagnetic forcing, *Journal of Geophysical Research: Atmospheres*, 112,  
<https://doi.org/10.1029/2006JD008306>, 2007.
- 430 Miyoshi, Y., Katoh, Y., Nishiyama, T., Sakanoi, T., Asamura, K., and Hirahara, M.: Time of flight analysis of pulsating aurora electrons,  
considering wave-particle interactions with propagating whistler mode waves, *Journal of Geophysical Research: Space Physics*, 115,  
2010.
- Miyoshi, Y., Oyama, S., Saito, S., Kurita, S., Fujiwara, H., Kataoka, R., Ebihara, Y., Kletzing, C., Reeves, G., Santolik, O., et al.: Energetic  
electron precipitation associated with pulsating aurora: EISCAT and Van Allen Probe observations, *Journal of Geophysical Research:*  
435 *Space Physics*, 120, 2754–2766, 2015.
- Nishimura, Y., Lessard, M. R., Katoh, Y., Miyoshi, Y., Grono, E., Partamies, N., Sivasdas, N., Hosokawa, K., Fukizawa, M., Samara, M.,  
et al.: Diffuse and pulsating aurora, *Space Science Reviews*, 216, 1–38, 2020.
- Nishitani, N., Ruohoniemi, J. M., Lester, M., Baker, J. B. H., Koustov, A. V., Shepherd, S. G., Chisham, G., Hori, T., Thomas, E. G.,  
Makarevich, R. A., et al.: Review of the accomplishments of mid-latitude Super Dual Auroral Radar Network (SuperDARN) HF radars,  
440 *Progress in Earth and Planetary Science*, 6, 1–57, 2019.
- Partamies, N., Juusola, L., Tanskanen, E., and Kauristie, K.: Statistical properties of substorms during different storm and solar cycle phases,  
*Annales Geophysicae*, 31, 349–358, <https://doi.org/10.5194/angeo-31-349-2013>, 2013.
- Partamies, N., Whiter, D., Kadokura, A., Kauristie, K., Nesse Tyssøy, H., Massetti, S., Stauning, P., and Raita, T.: Occurrence and average  
behavior of pulsating aurora, *Journal of Geophysical Research: Space Physics*, 122, 5606–5618, <https://doi.org/10.1002/2017JA024039>,  
445 2017.
- Tesema, F., Partamies, N., Nesse Tyssøy, H., Kero, A., and Smith-Johnsen, C.: Observations of electron precipitation during pulsating aurora  
and its chemical impact, *Journal of Geophysical Research: Space Physics*, p. e2019JA027713, <https://doi.org/10.1029/2019JA027713>,  
2020a.
- Tesema, F., Partamies, N., Nesse Tyssøy, H., and McKay, D.: Observations of precipitation energies during different types of pulsating aurora,  
450 *Annales Geophysicae Discussions*, pp. 1–18, 2020b.
- Thorne, R. M., Ni, B., Tao, X., Horne, R. B., and Meredith, N. P.: Scattering by chorus waves as the dominant cause of diffuse auroral  
precipitation, *Nature*, 467, 943, 2010.
- Turunen, E., Verronen, P. T., Seppälä, A., Rodger, C. J., Clilverd, M. A., Tamminen, J., Enell, C.-F., and Ulich, T.: Impact of different energies  
of precipitating particles on NO<sub>x</sub> generation in the middle and upper atmosphere during geomagnetic storms, *Journal of Atmospheric and*  
455 *Solar-Terrestrial Physics*, 71, 1176–1189, <https://doi.org/10.1016/j.jastp.2008.07.005>, 2009.



- Turunen, E., Kero, A., Verronen, P. T., Miyoshi, Y., Oyama, S.-I., and Saito, S.: Mesospheric ozone destruction by high-energy electron precipitation associated with pulsating aurora, *Journal of Geophysical Research: Atmospheres*, 121, 11,852–11,861, <https://doi.org/10.1002/2016JD025015>, 2016.
- 460 Verronen, P. T., Seppälä, A., Clilverd, M. A., Rodger, C. J., Kyrölä, E., Enell, C.-F., Ulich, T., and Turunen, E.: Diurnal variation of ozone depletion during the October–November 2003 solar proton events, *Journal of Geophysical Research: Space Physics*, 110, <https://doi.org/10.1029/2004JA010932>, 2005.
- Verronen, P. T., Andersson, M. E., Marsh, D. R., Kovács, T., and Plane, J. M. C.: WACCM-D—Whole Atmosphere Community Climate Model with D-region ion chemistry, *Journal of Advances in Modeling Earth Systems*, 8, 954–975, <https://doi.org/10.1002/2015MS000592>, 2016.
- 465 Watanabe, D. and Nishitani, N.: Study of ionospheric disturbances during solar flare events using the SuperDARN Hokkaido radar, *Advances in Polar Science*, 24, 12–18, 2013.
- Yang, B., Donovan, E., Liang, J., and Spanswick, E.: A statistical study of the motion of pulsating aurora patches: using the THEMIS All-Sky Imager, *Annales Geophysicae*, 35, 217–225, <https://doi.org/10.5194/angeo-35-217-2017>, 2017.
- 470 Yang, B., Spanswick, E., Liang, J., Grono, E., and Donovan, E.: Responses of Different Types of Pulsating Aurora in Cosmic Noise Absorption, *Geophysical Research Letters*, 46, 5717–5724, <https://doi.org/10.1029/2019GL083289>, 2019.